A Database of CFD-based Buffet Forcing Functions for Artemis I Structural Response Evaluation

Francesco Soranna[*], Craig L. Streett[†], Patrick S. Heaney[*], Martin K. Sekula[‡], David J. Piatak[§], Oleg O. Goushcha[*], and James M. Ramey[*]
NASA Langley Research Center, Hampton, VA 23681

Time-accurate FUN3D simulations are utilized to estimate buffet-induced unsteady forces experienced by the Space Launch System during the Artemis I (AR01) flight. A set of FUN3D simulations was developed that employed time-accurate mesh translations to simulate the changing velocity and attitude based on the AR01 best estimated trajectory. In these simulations, referred to as accelerating-flow simulations, the freestream Mach number increased from 0.80 to 1.92. Additional time-accurate simulations were obtained at constant freestream Mach number equal to 0.95, 1.18, 1.70, thereby simulating stationary conditions experienced by the flow in a wind-tunnel. On the grounds of favorable comparisons between simulated and flight-measured environments, the FUN3D-based surface pressures were utilized to develop a buffet forcing function (BFF) database. This BFF database was analyzed to characterize the spatial distribution and frequency content of the buffet forces during transonic and supersonic portions of the AR01 flight. The region of interest is located downstream of the forward attachment (FA) hardware between the core stage and the solid rocket boosters where vortex shedding off the FA protuberance produces significant unsteadiness. The analysis reveals that, at transonic and supersonic conditions, buffet forces that are based on constant M_∞ data are a good approximation of those based on accelerating-flow simulations.

Notice to Readers

The Space Launch System, including its predicted performance and certain other features and characteristics, have been defined by the U.S. Government to be Controlled Unclassified Information (CUI). Information deemed to be CUI requires special protection and may not be disclosed to an international audience. To comply with CUI restrictions, details such as absolute values have been removed from some plots and figures in this paper. It is the opinion of the authors that despite these alterations, there is no loss of meaningful technical content. Analytical methodologies and capabilities are discussed, significant and interesting technical results are still present, and meaningful conclusions are presented.

Acronyms

AR01	=	Artemis I	LSRB	=	Left Solid Rocket Booster
BET	=	Best Estimated Trajectory	PSD	=	Power Spectral Density
CFD	=	Computational Fluid Dynamics	OML	=	Outer Mold Line
BFF	=	Buffet Forcing Function	RSRB	=	Right Solid Rocket Booster
DFI	=	Developmental Flight Instrumentation	SLS	=	Space Launch System
FA	=	Forward Attachment	SRB	=	Solid Rocket Booster
KDE	=	Kernel Density Estimation			

[*]Research Aerospace Engineer, Aeroelasticity Branch, AIAA Member.
[†]Senior Research Scientist, Computational Aerosciences Branch.
[‡]Senior Research Aerospace Engineer, Aeroelasticity Branch.
[§]Assistant Branch Head, Aeroelasticity Branch, AIAA Senior Member.

Nomenclature

C'_p = fluctuating pressure coefficient
D = core stage diameter, in
dx = longitudinal spacing
$d\hat{x}$ = nondimensional longitudinal spacing (normalized by D)
$d\theta$ = azimuthal spacing
$()_{\text{eff}}$ = effective conditions
f_i = sectional force (force-per-length), lbf/ft
f = frequency, Hz
F = point force, lbf.
$()_i$ = axes indices
$()_j$ = an index
$()_k$ = an index
M_∞ = freestream Mach number
M_{initial} = initial freestream Mach number for an accelerating-flow simulation
q = dynamic pressure, psf
rms = root mean square
$()_{\text{ref}}$ = reference conditions
$()_{x,y,z}$ = longitudinal, lateral, vertical vehicle axes
$\hat{x}$ = nondimensional length, x/D
α = angle of attack, deg.
β = sideslip angle, deg.
γ = coherence function
θ = body coordinate system clocking angle, deg.
Φ = power spectral density

I. Introduction

The Space Launch System (SLS) is NASA's newest super heavy-lift rocket designed for deep space exploration and Artemis [1]. Figure 1 shows, from left to right, the evolution of the SLS Crew and Cargo configurations in increasing order of lift capabilities [2]. In this figure, the configuration shown on the far left is the SLS Block 1 Crew configuration that was flown during Artemis I (AR01). The AR01 test flight was a successful uncrewed Moon-orbiting mission that launched on November 16, 2022 from the NASA Kennedy Space Center in Cape Canaveral, Florida [3].

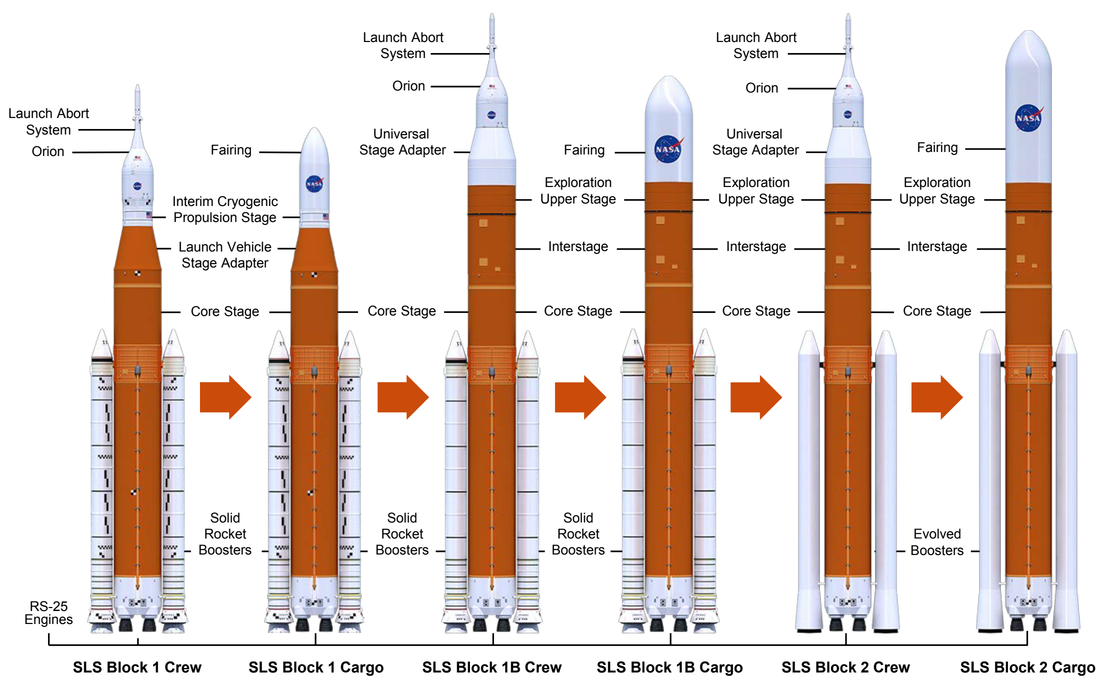

Fig. 1 SLS vehicle configurations.

During ascent, transonic buffet is a major source of structural excitation on the Space Launch System. To give an idea of the order of magnitude of this excitation, in sections of the liquid hydrogen tank, peak buffet conditions produce fluctuating forces on the order of tens of thousands of pounds (root-mean-square). The spectra of these buffeting forces may contain both high-energy broadband frequency content as well as narrowband frequency content. Since these excitation spectra could excite resonance frequencies of the vehicle and its components, it is paramount that transonic buffet forces are well characterized and accounted for in the design phase.

The present paper continues efforts by the same authors to generate high-fidelity databases of buffet forcing functions (BFFs) in support of the SLS design (Refs. [4–6]). Up to this point, these BFF databases are based on wind-tunnel data that provide a reasonable characterization of the flight environments [7, 8]. However, utilizing wind-tunnel test data for BFF development presents assumptions and limitations, some of which are discussed next.

Typically, launch vehicle buffet testing in wind tunnels is focused on transonic and low supersonic Mach number conditions where the peak buffet environment is expected. However, the Artemis I flight revealed that specific buffet-induced responses persist above the range of Mach numbers tested during buffet wind-tunnel tests. Another important limitation is an approximate order of magnitude difference in Reynolds number between a wind-tunnel test and the corresponding full-scale vehicle in flight.

Furthermore, wind-tunnel experiments are based on stationary flow conditions, whereas the flow around a rocket is nonstationary due to vehicle acceleration through the atmosphere. As an example, the AR01 flight test vehicle accelerated between Mach=0.80 and Mach=1.92 in approximately 30 seconds. In a wind tunnel, the freestream Mach number can not be changed at a rate equivalent to flight, which is considerably faster. In the AR01 example, for a 2.5% scale model test in a wind tunnel, the equivalent time scale to accelerate the flow between Mach=0.80 and Mach=1.92 is 0.75 seconds (assuming the same velocities between flight and wind-tunnel conditions). Therefore, testing in a wind tunnel is conducted at constant freestream conditions. As yet another limitation, the discrete and limited pressure measurements obtained from wind tunnel tests introduce uncertainty in the BFF estimation process.

While flight tests of launch vehicles are invaluable in that they remove some of the above-mentioned limitations, instrumenting launch vehicles with a sufficient number of sensors for buffet applications is seldom done (Refs. [9–11]) and subject to sensor loss. Furthermore, flight data contain nonbuffet related aerodynamic excitation inputs, such as gust excitation and acoustics, that can be difficult to isolate from buffet [9]. Advanced computational fluid dynamics (CFD) provides a viable means to fill some of the gaps existing in the experiments and to separate the impact of different excitation contributors.

The present work has two objectives. The first is to establish a level of confidence in the ability of CFD to estimate buffet-related environments under flight-like conditions. The second objective is to utilize these CFD data to develop a database of buffet forces that is representative of flight-like conditions, including vehicle-acceleration effects up to a supersonic Mach regime. One aspect of particular interest is to address how well flight-like BFFs compare to their stationary flow analog.

To meet these objectives, the first part of the paper compares CFD unsteady pressures to those measured during AR01 flight test. Then, on the basis of favorable comparisons between simulated and flight-measured environments, the CFD-based surface pressures are integrated into fluctuating forces acting on the vehicle. Such forces form the basis of a CFD-based BFF database. Comparisons are drawn between BFFs from accelerating vs. constant Mach number conditions.

II. FUN3D Flow Simulations

FUN3D [12] is a NASA-developed CFD code, with the capability for accurate eddy-resolving simulations having been demonstrated in a number of studies dating back to 2015 (Ref. [13]). These studies involved simulation of unsteady surface pressures for prediction of buffet and aeroacoustics of launch vehicles and other configurations, including quantitative comparison with detailed wind-tunnel tests.

The mesh and computational parameters used in the AR01 accelerating flight simulation generally followed best practices derived from those prior campaigns. Due to computational considerations related to mesh size, the Block 1 Cargo forebody (see Fig. 1, second configuration from the left), rather than the AR01 Block 1 Crew (shown in Fig. 1, first configuration from the left), was used in this simulation. For unsteady pressure environments in the multibody (core and solid rocket boosters) region of interest for this database, the effect of the forebody has generally been observed to be minimal.

An image of the surface mesh utilized in this FUN3D database is shown in Fig. 2. In this figure, regions colored in blue show surfaces where pressures from the FUN3D simulations are collected for database development. These surfaces correspond to: (1) core stage segments with full-azimuthal coverage, including the forward skirt, liquid oxygen tank, intertank, and liquid hydrogen tank, and (2) forward region on the left and right solid rocket boosters in the vicinity of the forward attachment to core, with partial azimuthal coverage on surfaces facing the booster-to-core gaps.

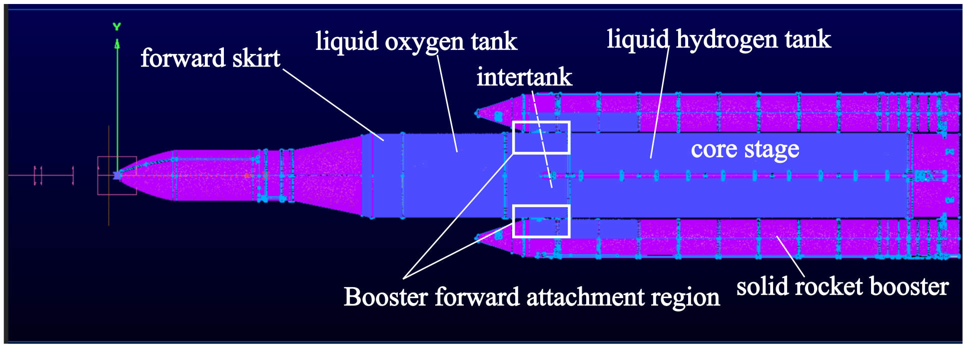

Fig. 2 SLS Block 1 Cargo surface mesh utilized in this FUN3D database.

The simulation utilized the improved delayed detached-eddy (iDDES) turbulence model, with the Spalart-Allmaras (SA-neg) RANS model. The time-accurate mesh translations were also utilized to simulate the changing velocity and attitude based on the AR01 best estimated trajectory (BET). Note that this method of simulating an accelerating trajectory does not account for farfield condition changes along the trajectory; in particular, speed of sound and Reynolds number are held constant based on the initial conditions of the simulation.

Two accelerating-flow simulations were carried out corresponding to a low and a high freestream Mach number (M_∞) range. Table 1 summarizes the M_∞ range for these two simulations and the corresponding flight duration in the BET. For each range, the accelerating-flow simulation is carried out first by running a time-accurate simulation at an appropriate initial freestream Mach number, M_{initial}, that corresponds to the lower bound of each accelerating-flow simulation. Therefore, for the low M_∞ range, $M_{\text{initial}} = 0.80$, and for the high M_∞ range, $M_{\text{initial}} = 1.25$. The initial stationary flow simulations are run until the simulation reaches a statistically-steady state and the resulting flowfield is then used to initialize the accelerating-flow simulations, with careful modification of the evolving coordinate transforms in the initial time period to avoid large starting transients. In these FUN3D simulations, the vehicle attitude is set according to the AR01 BET angle of attack, α, and sideslip angle, β, shown in Fig. 3. Figure 4 shows a comparison of trajectory M_∞ between the FUN3D simulation and the BET. This comparison is shown only for the high M_∞ range. Slight deviations between FUN3D and flight are present as the simulation time progresses due to the assumption of constant speed-of-sound in the velocity-based accelerating simulation.

As the accelerating-flow framework assumes a constant farfield atmosphere, the effective dynamic pressure, q_{eff}, for an accelerating-flow simulation at M_∞ is:

$$q_{\text{eff}} = \frac{1}{2}\,\rho_{\text{ref}}\,a_{\text{ref}}^2\,M_\infty^2 = q_{\text{ref}}\left(\frac{M_\infty}{M_{\text{ref}}}\right)^2 \tag{1}$$

where ρ is density, a is the speed-of sound, and the subscript "ref" refers to reference conditions, here corresponding to the initial conditions for each Mach number range of Table 1. Assuming that static pressure scales linearly with dynamic pressure, the FUN3D-computed static pressure must be corrected according to:

$$p = p_{\text{FUN3D}}\,\frac{q(M_\infty)}{q_{\text{eff}}} \tag{2}$$

where p_{FUN3D} is the static pressure computed during the FUN3D accelerating-flow simulation and $q(M_\infty)$ is the dynamic pressure at M_∞ based on the BET.

In order to compare the effects of accelerating-flow vs. stationary conditions on the buffet forcing functions, additional FUN3D stationary flow simulations were conducted at constant freestream Mach numbers, $M_\infty = 0.95, 1.18,$ and 1.70. Table 2 compares attitude conditions between accelerating-flow and constant M_∞ simulations. For constant M_∞ simulations, the attitude is set to zero degrees except for the $M_\infty = 1.18$ simulation where α and β are based on the BET. All the FUN3D simulations presented here were conducted at wind-tunnel scale Reynolds numbers where FUN3D simulations were previously validated against wind-tunnel data.

Table 1 Freestream Mach number range for FUN3D accelerating-flow simulations and the corresponding AR01 I flight duration according to the BET.

	M_∞	BET initial time, sec.	BET final time, sec.	flight duration, sec.
low range	[0.80, 1.26]	45.2	61.95	16.75
high range	[1.25, 1.92]	60.5	74.0	13.5

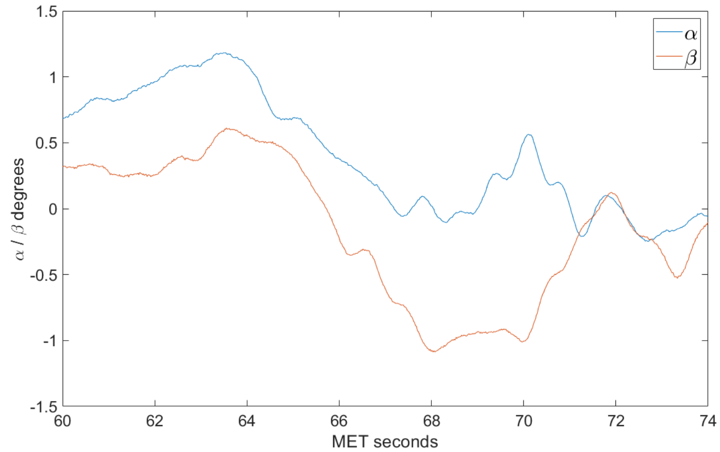

Fig. 3 AR01 flight attitude utilized in the accelerating-flow FUN3D simulation.

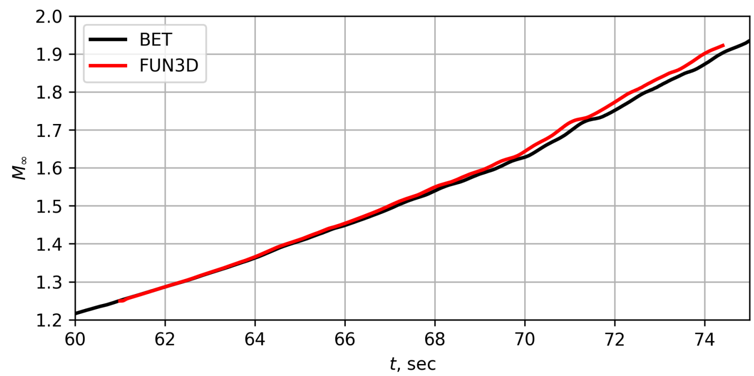

Fig. 4 Comparison of M_∞ for the accelerating-flow FUN3D simulation and AR01 BET.

Table 2 FUN3D simulations α and β at reference M_∞ values presented in this paper. Angles shown in degrees. Conditions shown in bold are matched to the BET.

Mach number	constant-M_∞ α, β (deg.)	accelerating-flow α, β (deg.)
0.95	0.0, 0.0	**0.2, 0.4**
1.18	**0.5, 0.1**	**0.5, 0.1**
1.70	0.0, 0.0	**0.0, -0.3**

III. Results

In the first part of this section, sample fluctuating pressure data from FUN3D accelerating-flow simulations of the AR01 flight are presented. Root-mean-square and spectrograms of the FUN3D fluctuating pressures are compared to AR01 flight data from developmental flight instrumentation (DFI). In the second part of this section, results from integrating the FUN3D fluctuating pressures into buffet forcing functions are presented.

As a reference, Fig. 5 shows the SLS body coordinate systems utilized in the analysis that follows, where, for each body, x is the longitudinal axis, y is the lateral axis, z is orthogonal to the xy plane based on the right-hand rule, and θ is the body coordinate system azimuthal angle. Figure 6 presents core stage stations following a numbering convention based on AR01 and wind-tunnel test instrumentation. These stations will be referred to later on in the context of presenting buffet forcing functions results. The analysis focuses downstream of the forward attachment (FA) region (Fig. 6). A closeup view of a wind-tunnel representation of the FA protuberance connecting the core and left solid rocket booster is shown in Fig. 7.

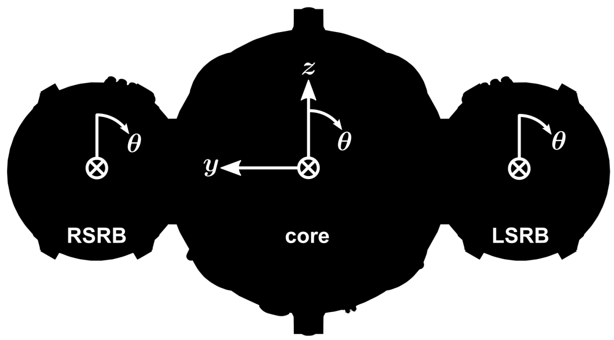

Fig. 5 Body coordinate systems on the core and on the left/right side solid rocket boosters, LSRB/RSRB. View in the aft-facing, +x, direction.

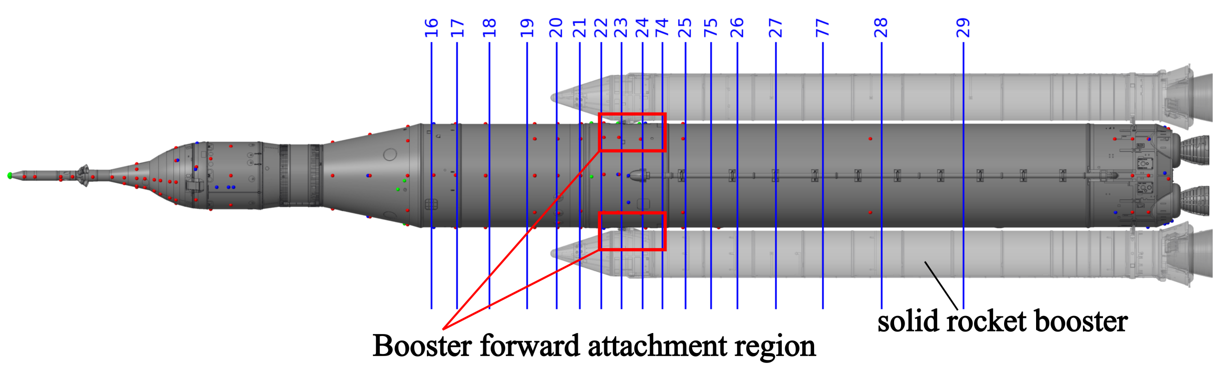

Fig. 6 Core BFF stations.

A. Comparison of Fluctuating Pressures, Simulation to Flight

During the Artemis I flight, fluctuating pressure data from 183 DFI sensors were acquired throughout ascent to observe the external unsteady pressure environments and to compare with preflight predictions based on wind-tunnel testing [11, 14]. While the flight environments compared favorably with predictions in many regions of the vehicle, significant differences were observed in the multibody region where the solid rocket boosters (SRBs) attach to the core stage. These differences between wind tunnel and flight data include estimates of the spatial extent of peak unsteadiness downstream of the forward attachment and the narrowband frequencies of unsteady pressure modes.

To help understand these differences, and as a validation step prior to a CFD-based database development, the accelerating-flow FUN3D surface pressures are compared to those measured by pressure transducers installed on the AR01 flight test vehicle. Data from four flight sensors annotated in Fig. 8, are compared to data from the accelerating-flow

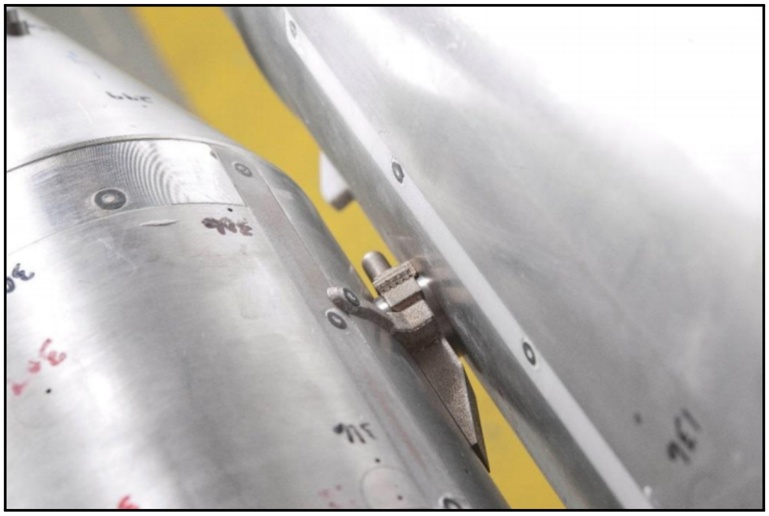

Fig. 7 SLS booster forward attachment hardware.

simulation. Analysis locations 1 to 3 corresponds to sensors located on the core at $z = 0$ (Fig. 5) in the gap between the left SRB (LSRB) and the core stage, and analysis location 4 corresponds to a sensor on the core located in the gap between the right SRB (RSRB) and the core stage.

Representative time histories of the mean-removed pressure coefficient, C_p', versus the freestream Mach number, M_∞, are plotted in Fig. 9 for the AR01 flight sensor located at analysis location 3 and the nearest neighbor CFD node. The vehicle body coordinate system and clocking angle, θ, are also illustrated for reference (see also Fig. 5). Data from both flight and CFD are bandpass filtered from 0.5 to 100 Hz, and then processed to compare the total energy in this bandwidth (using root mean square) as well as the time-frequency distribution.

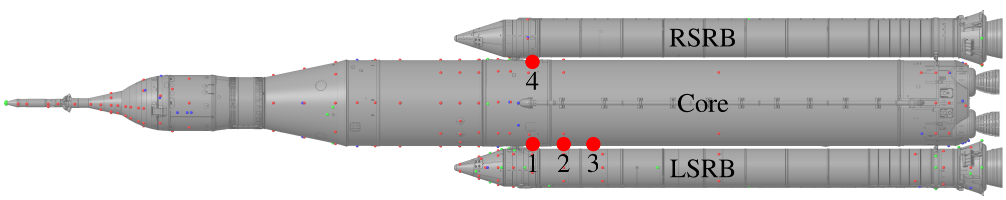

Fig. 8 Artemis I flight vehicle with annotated analysis locations of unsteady pressure transducers discussed in this study.

Using a window duration of 0.5 s, Fig. 10 presents the moving window root-mean-square (rms) of the detrended pressure coefficient, $C'_{p,\text{rms}}$, for data at the four analysis locations. In comparison to the flight data, the simulation trends for each location compare favorably with respect to M_∞ as well as in the flight-measured increase in unsteady energy in this bandwidth traveling aft in the LSRB-Core gap downstream of the FA from analysis locations 1 to 3.

Comparisons of the time-frequency distribution of unsteady pressure energy are shown in Fig. 11, where time axes have been mapped to M_∞ and the flight and simulation spectrograms are presented in the left and right columns, respectively. In each plot, the M_∞ and frequency axes have the same range and resolution. At each analysis location, the AR01 and CFD spectrograms demonstrate broadly similar features, in particular: (1) relatively constant frequency peaks corresponding to unsteady pressure modes in the lower supersonic flight ($M_\infty \in [1.2, 1.7]$) and (2) rapid increase in these frequency peak ridges at approximately $M_\infty = 1.7$. These features were not as well represented in the preflight wind-tunnel test data [7].

In addition to analyzing the fluctuating pressure characteristics at discrete locations, comparisons of the relationships between data at those locations is important to improve understanding of the coherent flow features and unsteady pressure modes that may efficiently excite vehicle structural responses and loads. For both the AR01 and CFD data, the coherence function, γ, between windowed time histories for pairs of sensors are shown in Fig. 12. In these plots, the time histories have been subset within $M_\infty \in [1.675, 1.725]$ for a total window size of $\Delta M_\infty = 0.05$. In Fig. 12a,

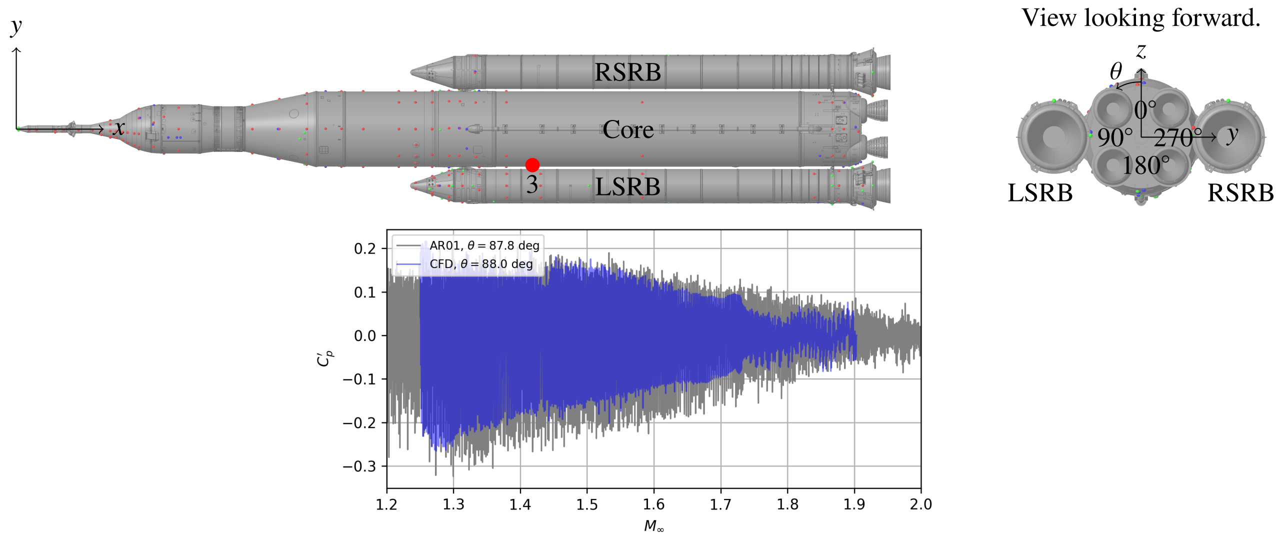

Fig. 9 Comparison of bandpass filtered C_p' versus M_∞ for the AR01 flight sensor at analysis location 3 and the nearest neighbor CFD node.

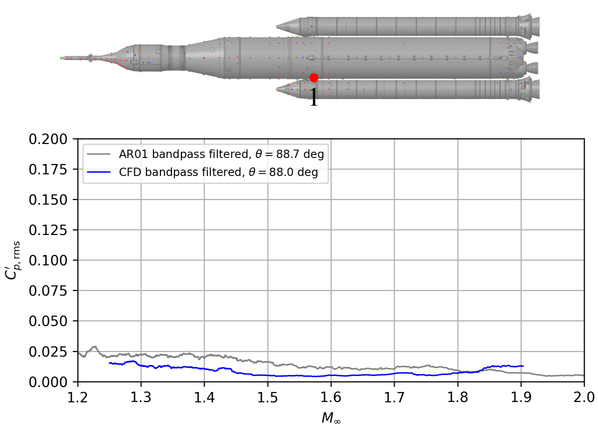

(a) Analysis location 1, LSRB-Core gap.

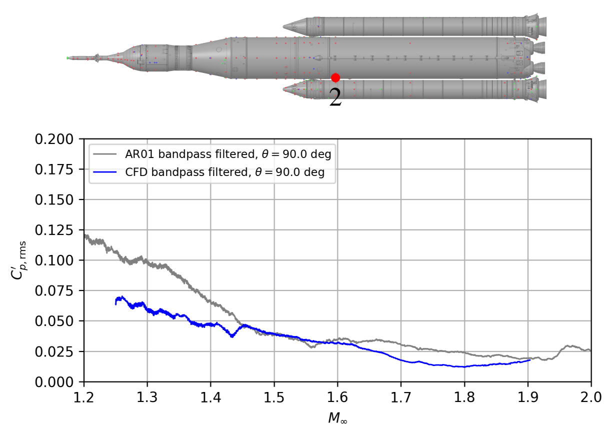

(b) Analysis location 2, LSRB-Core gap.

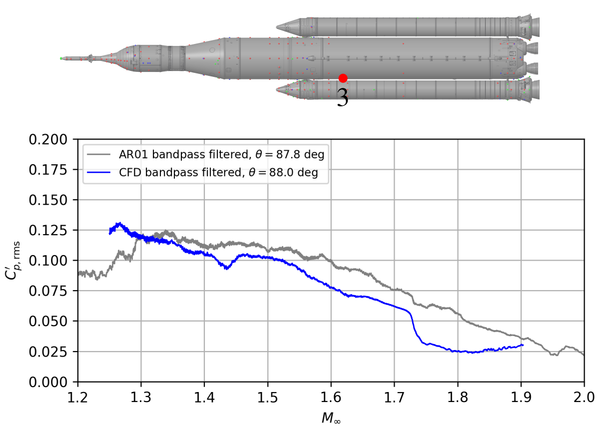

(c) Analysis location 3, LSRB-Core gap.

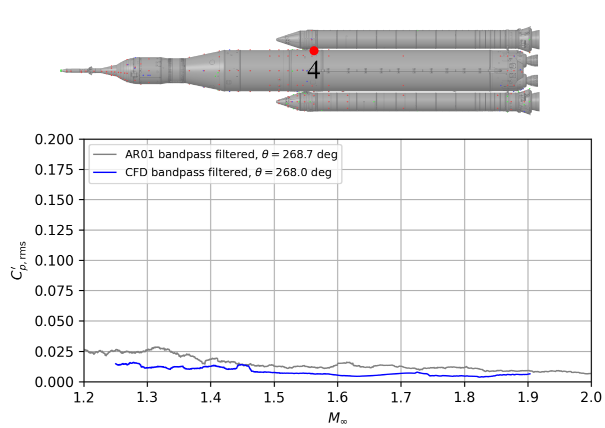

(d) Analysis location 4, RSRB-Core gap.

Fig. 10 Comparison of bandpass filtered $C'_{p,\mathrm{rms}}$ versus M_∞ for AR01 flight sensors at analysis locations and the corresponding nearest neighbor CFD nodes.

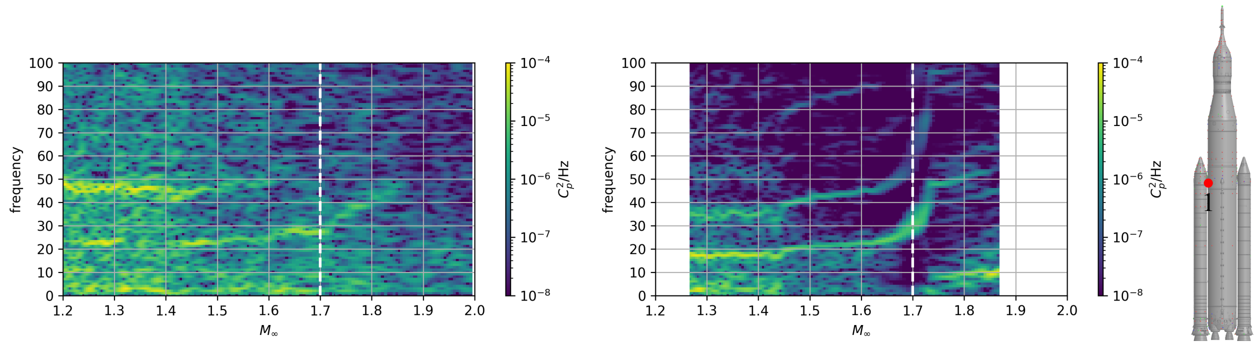

AR01. **CFD.**

(a) Analysis location 1.

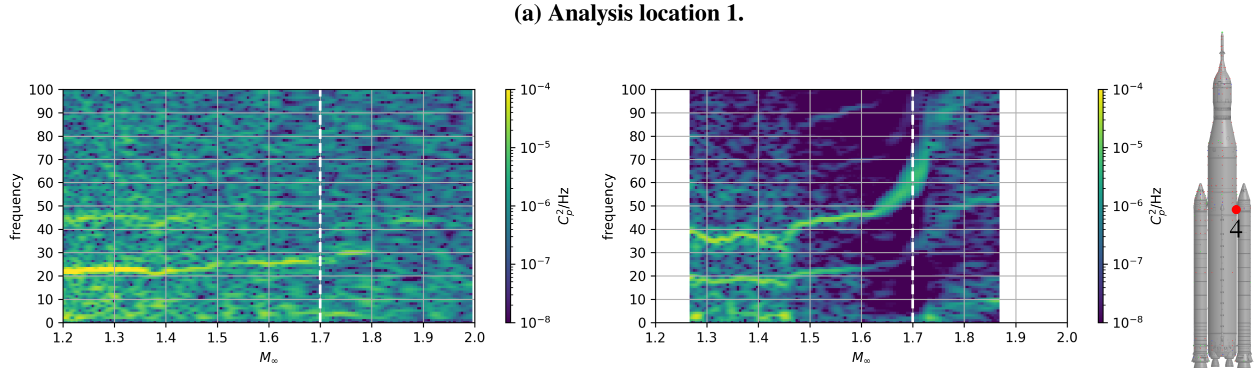

AR01. **CFD.**

(b) Analysis location 4.

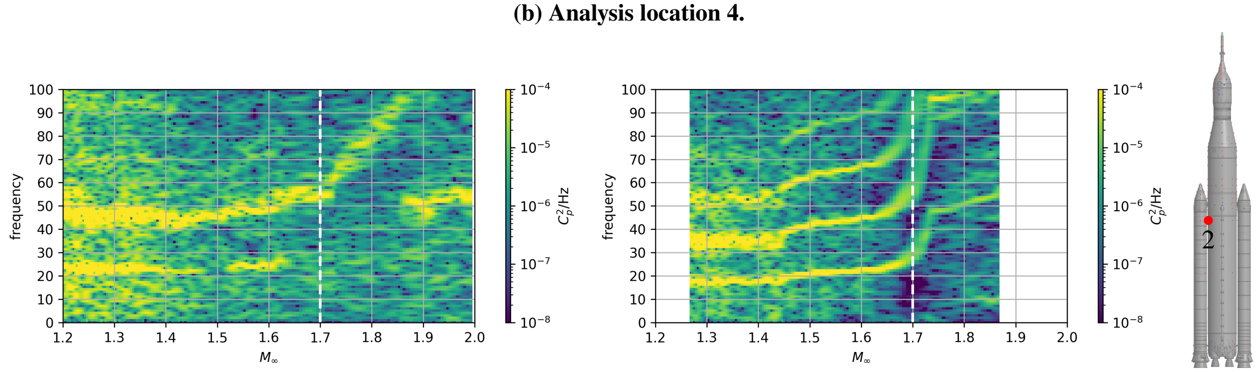

AR01. **CFD.**

(c) Analysis location 2.

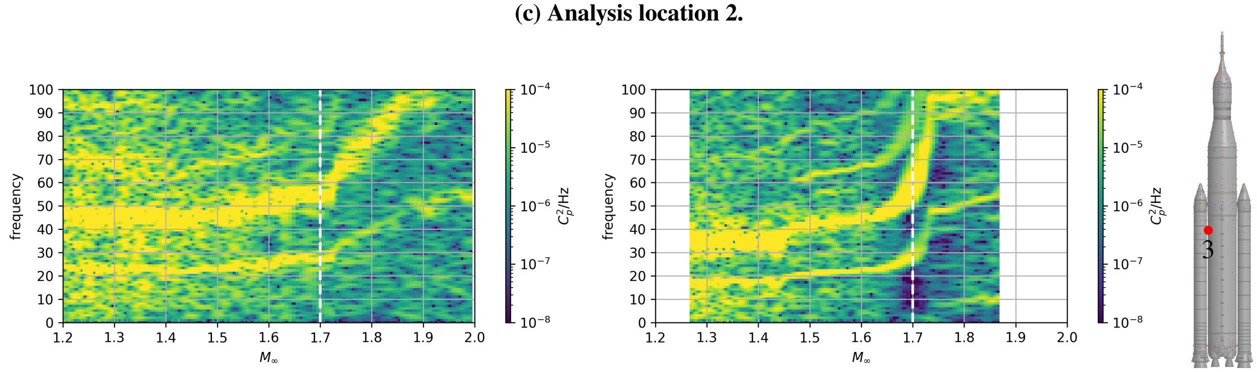

AR01. **CFD.**

(d) Analysis location 3.

Fig. 11 Comparison of C_p' time-frequency spectrograms versus M_∞ for AR01 flight sensors at analysis locations and the corresponding nearest neighbor CFD nodes.

where coherence relationships for sensor pairs located in the LSRB-core gap are shown, high coherence between sensor pairs is present for both the AR01 and CFD data at the peak frequencies corresponding to the unsteady pressure modes (seen as the frequency ridges in Fig. 11, where $M_\infty = 1.7$ is indicated with a vertical dashed line). In the legend, the nondimensional distances between sensor pairs j and k, $d\hat{x}_{j,k} = dx_{j,k}/D$ (D is the reference core stage diameter), are indicated for reference. For the CFD data, coherence is relatively high for broader frequency ranges around these peaks, potentially due to the rapid changes in the frequency peak ridges around this Mach number shown in Fig. 11 relative to the AR01 flight data.

In Fig. 12b, where coherence relationships for sensor pairs located on either side of the core are shown, sensor-to-sensor coherence is relatively low due to the physical separation between analysis locations and small differences between the peak frequencies on either side of the core, which provides some evidence that the interaction between unsteady pressure modes on either side of the core is not high. Similar to the comparison for longitudinally-arranged sensor pairs, the CFD coherence for sensors on opposite sides of the core is higher for broader frequency ranges than for the AR01 data, which may be due to the rapid changes in the frequency peak ridges and the challenge of applying stationary signal analysis tools to nonstationary signals.

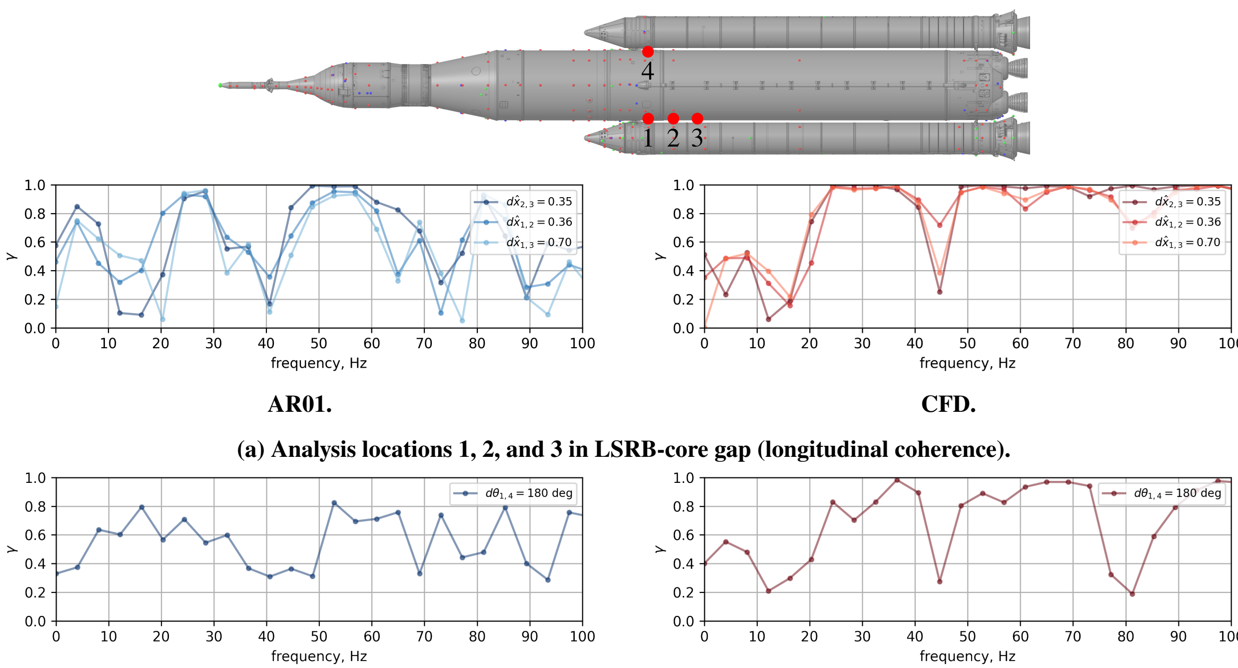

AR01.

CFD.

(a) Analysis locations 1, 2, and 3 in LSRB-core gap (longitudinal coherence).

AR01.

CFD.

(b) Analysis locations 1 and 4 on opposite sides of core.

Fig. 12 Comparison of coherence between pairs of time histories for AR01 flight sensors at analysis locations and the corresponding nearest neighbor CFD nodes for $M_\infty \in [1.675, 1.725]$.

B. Fluctuating Sectional Forces Root-Mean-Square Trends.

Let F_i define the fluctuating component of a point force acting along the i-axis on the centerline of the core stage or on the boosters' centerline. A fluctuating sectional force is defined as $f_i(x,t) = dF_i/dx$, where t is time and dx is an arbitrarily small spacing between longitudinal planes on each body. From now on, both F_i and f_i are referred to as buffet forcing functions, either point BFFs (F_i) or sectional BFFs (f_i). Focusing on the core stage, f_i were calculated at 261 longitudinal locations (for brevity, boosters' BFFs are not presented in this paper, but they were analyzed). The spacing dx between these 261 longitudinal locations is $dx/D = 0.025$, where D is the reference core stage diameter.

Figures 13-15 present distributions of rms values of the fluctuating sectional force, f_i, acting on the core stage in the booster-to-booster direction $i = y$ (left column) and in the out-of-plane direction $i = z$ (right column), as defined in Fig. 5. Each figure corresponds to a sample M_∞ chosen to represent: a near peak-buffet condition, $M_\infty = 0.95$ (Fig. 13);

the highest Mach number for transonic wind-tunnel testing, $M_\infty = 1.18$ (Fig. 14); and a higher supersonic condition, $M_\infty = 1.70$ (Fig. 15) in which the AR01 flight-data revealed a nonnegligible buffet environment. All the plots of Figs. 13-15 share the same y-axis range, obtained by dividing the rms values by the same arbitrary constant. The labels on the x-axis are sample vehicle station numbers that are a subset of those shown in Fig. 6. Each rms plot contains data from accelerating-flow simulations (blue curve) and constant M_∞ simulations (red curve). Prior to computing the rms, the sectional force data were detrended and band-pass filtered within the frequency range $f \in [0.5, 100]$ Hz.

In order to compare data between accelerating-flow and constant M_∞ simulations, a windowing approach was utilized. Utilizing accelerating-flow simulations data, $f_{i,\mathrm{rms}}$ values at each longitudinal location are computed for f_i samples within a $M_\infty \pm 0.01$ window centered around each specific M_∞. For example, for the $M_\infty = 0.95$ case, $f_{i,\mathrm{rms}}$ is computed for f_i samples within $M_\infty \in [0.94, 0.96]$. For reference, Table 3 shows, in the second column, the record length for three M_∞ windows based on accelerating-flow simulations. These record lengths for the M_∞ windows are a close approximation of their BET-based counterparts, where small deviations from the BET-estimated M_∞ windows are due to constant farfield assumptions in FUN3D. It is important to note that the M_∞ window record-lengths of Table 3 get smaller with M_∞, due to the prescribed trajectory profile of the vehicle. As discussed in the next section, increasingly small record lengths pose restrictions on the BFFs spectral content derived from accelerating-flow data.

Table 3 Comparisons of record lengths for FUN3D simulations. 2nd column: M_∞ windows for accelerating-flow simulations, 3rd column: full record length for constant M_∞ simulations.

	record length (sec.)	
M_∞	accelerating flow	constant M_∞
0.95	0.767	25.1
1.18	0.592	26.5
1.70	0.220	16.7

For a constant M_∞ simulation, in order to achieve a statistically converged steady-state solution, the simulation is run over much longer record lengths, as shown in Table 3, third-column. For these constant M_∞ simulations, $f_{i,\mathrm{rms}}$ are computed based on an ensemble average of a moving window standard deviation of f_i samples. Note that the record length of a rms moving window for constant M_∞ data corresponds to the record length of the corresponding accelerating-flow M_∞ window. For example, at $M_\infty = 0.95$, the rms moving window size corresponds to 0.77 seconds (Table 3). An estimation of the probability distribution of the $f_{i,\mathrm{rms}}$ realizations for constant M_∞ data was made based on a kernel density estimation method (KDE) described in Ref. [15]. In Figs. 13-15, the probability distributions of $f_{i,\mathrm{rms}}$ are shown by violin plots (Ref. [16]) at sample locations (green patches).

As expected based on AR01 and wind-tunnel data [8], $f_{i,\mathrm{rms}}$ are highest at transonic condition, $M_\infty = 0.95$, (Fig. 13) and decrease by a factor of ~ 2.0 at $M_\infty = 1.70$ (Fig. 15). Focusing on the $M_\infty = 0.95$ condition, the peak buffet environment is located between stations 25 and 26. This significant buffet environment is associated with vortex shedding off the attachment hardware that connects the solid rocket boosters to the core stage (marked in Fig. 2, see also Fig. 6). This phenomenon initiates at station 23 (marked in Fig 6 and on the x-axis in Figs. 13-15). An extensive study related to this environment is documented in the literature (Ref.[13]).

Comparing accelerating-flow data (blue) vs. constant $M_\infty = 0.95$ data (red), Fig. 13 reveals that $f_{i,\mathrm{rms}}$ levels are in close agreement based on these simulations, with a notable exception. Upstream of station 23, the accelerating-flow simulation estimates higher $f_{i,\mathrm{rms}}$ vs. constant M_∞ data (this difference is under investigation). Another observation related to the constant $M_\infty = 0.95$ case is that the violin plots display a significant level of $f_{i,\mathrm{rms}}$ variability, hence variability in buffet behavior, between stations $25 - 26$, despite constant freestream assumptions. Increasing the M_∞ window size from ± 0.01 to ± 0.02 tends to reduce this $f_{i,\mathrm{rms}}$ variability by a small amount.

For the supersonic conditions presented in Figs. 14-15, the impact of accelerating flow on $f_{i,\mathrm{rms}}$ is very small as shown in these plots by the red and blue curves being nearly coincident. One last observation is that, in all the plots of Figs. 13-15, $f_{i,\mathrm{rms}}$ peaks located downstream of station 26 are caused by shocks generated by the boosters field joints impinging on the core OML.

C. Power Spectra Density of Fluctuating Sectional Forces

This section extends comparisons presented in the previous section to analyzing the spectral content of f_i based on both constant M_∞ and accelerating-flow simulations. To compute the power spectral density (PSD) Φf_i, the

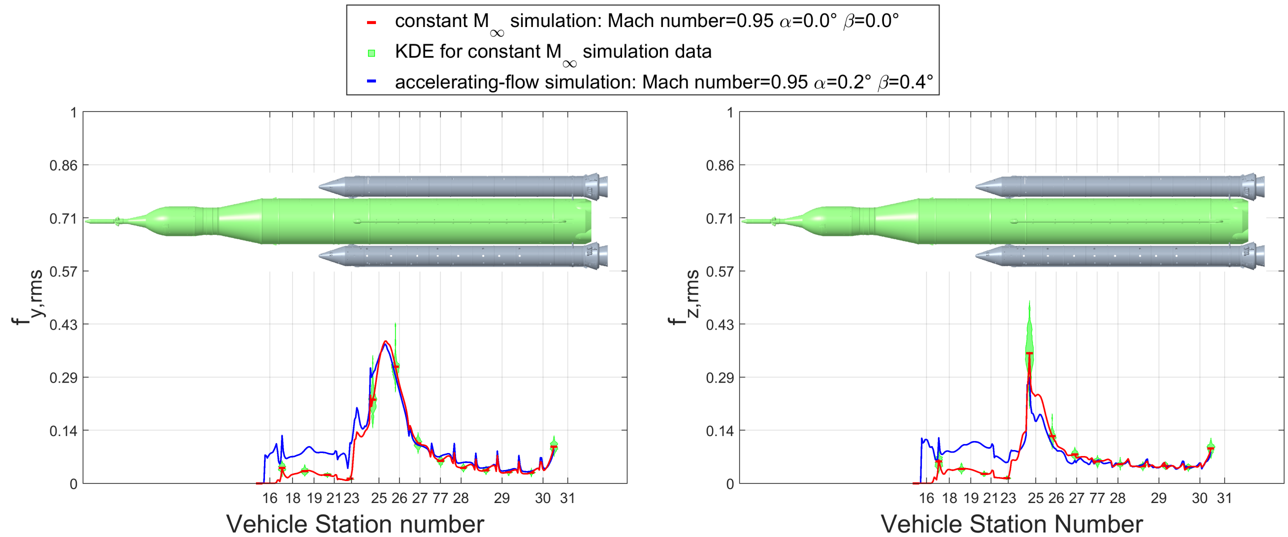

Fig. 13 Band-passed filtered rms trends of $f_{y,z}$ on the core stage from FUN3D constant M_∞ data and accelerating-flow simulation data windowed around M_∞ = 0.95.

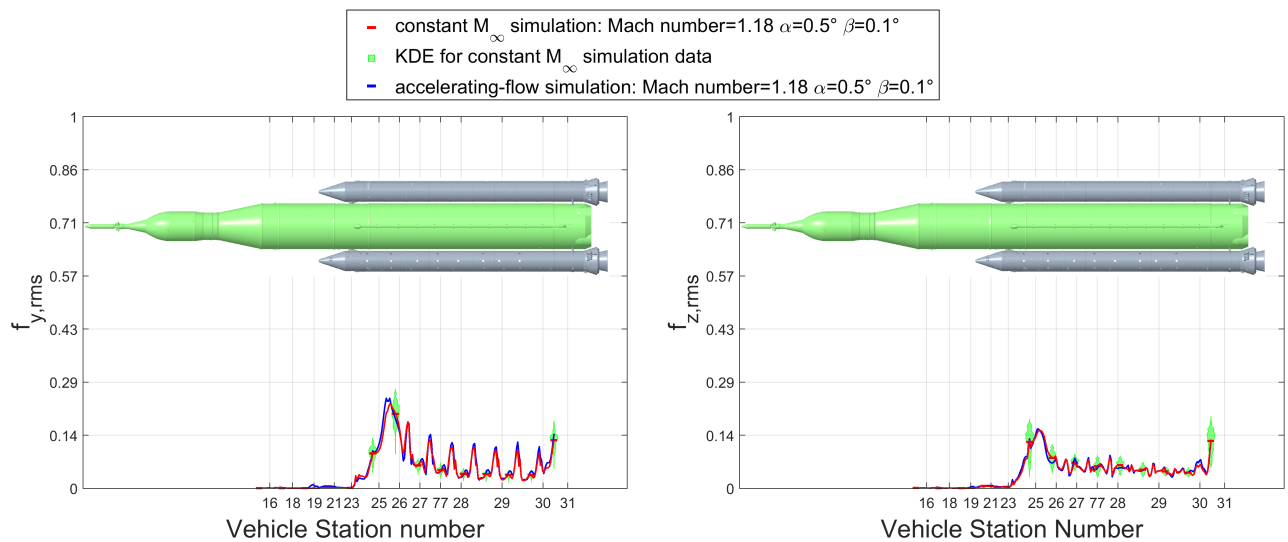

Fig. 14 Band-passed filtered rms trends of $f_{y,z}$ on the core stage from FUN3D constant M_∞ data and accelerating-flow simulation data windowed around M_∞ = 1.18.

MATLAB™ implementation of the Welch's method is employed. Starting with accelerating-flow data, f_i data segments are selected based on $M_\infty \pm 0.01$, where $M_\infty \in \{0.95, 1.18, 1.70\}$, as described in the previous section. Then, the size of the window in Welch's method is set to the number of samples contained within each f_i data segment. As a result, for accelerating-flow data, each M_∞ PSD is based on a single f_i data segment and the PSD frequency resolution corresponds to the inverse of the record length shown in Table 3, second column. While a single data segment maximizes the PSD frequency resolution, this choice comes at the expense of the PSD accuracy, particularly for higher frequency.

For constant M_∞ data, the PSD window size is set in order to match the length of the corresponding accelerating-flow simulation M_∞ segment listed in Table 3, second column. Hence, Φf_i based on constant M_∞ data and accelerating-flow data share the same frequency resolution. In the case of constant M_∞ data, owing to longer record lengths compared to

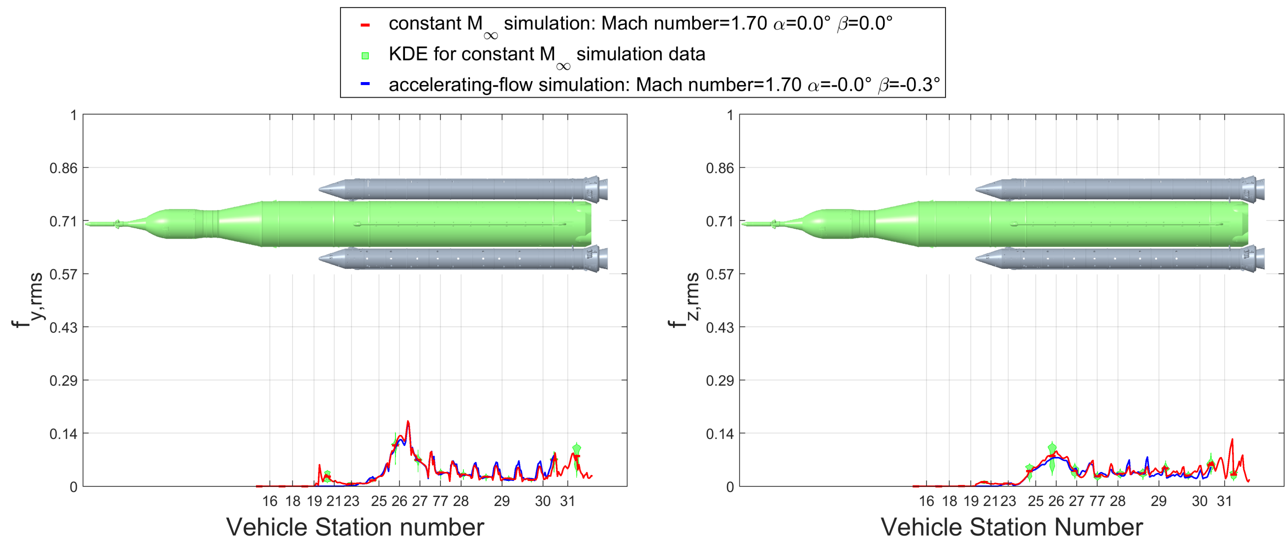

Fig. 15 Band-passed filtered rms trends of $f_{y,z}$ on the core stage from FUN3D constant M_∞ data and accelerating-flow simulation data windowed around M_∞ = 1.70.

accelerating-flow data, Φf_i is an ensemble mean PSD resulting from multiple data segments.

Figures 16-18 present comparisons $\Phi f_{y,z}$ based on constant M_∞ and accelerating-flow simulations at sample locations on the core stage within the peak buffet environments, stations 25-26, and at station 77 located just downstream of the peak buffet location (see Fig. 6 for an illustration of these stations). In each figure, the top row shows Φf_y and the bottom row Φf_z. The red curve is based on constant M_∞ data, while the blue curve is based on accelerating-flow data. In addition, the gray patch represents a PSD range for constant M_∞ data, obtained by holding, at each frequency, the maximum and minimum $\Phi f_{y,z}$ values among the ensemble realizations. In each plot, the frequency range is limited up to 100 Hz, while the frequency resolution is dictated by the record length of the M_∞ window for each specific freestream Mach number (Table 3). As a result, the $M_\infty = 1.70$ case displays the lowest frequency resolution (4.55 Hz). The blue labels on the plots of Figs 16-18 annotate the frequency of peak $\Phi f_{y,z}$ across the spectrum, based on accelerating-flow data.

From the plots in Figs. 16-18, the power spectral densities based on the two data sources, constant M_∞ vs. accelerating-flow data, share the same levels and trends. Accelerating-flow Φf_i are mostly bounded by an ensemble PSD range based on constant M_∞ data, as shown by comparing the blue curves to the gray patches. However, Φf_i deviations are seen at $M_\infty = 0.95$ and $M_\infty = 1.18$ below 5 Hz (Figs. 16-17). At $M_\infty = 1.70$, below 10 Hz, Φf_i based on accelerating-flow data is less than the bounds of the constant M_∞ PSD range. Also at $M_\infty = 1.70$, accelerating-flow Φf_y exceedences exist near 27 Hz as discussed in more detail at the end of this section.

At $M_\infty = 0.95$ (Fig. 16), only Φf_z spectra based on constant M_∞ data (red lines, bottom row) show a clear narrowband content around 10.4 Hz that is likely associated with a subharmonic of vortex shedding off the FA protuberance. For the low supersonic case, $M_\infty = 1.18$ (Fig. 17), Φf_y shows distinct 40.5 Hz peaks at the three sample stations. These peaks are associated with vortex shedding off the FA hardware, which, in the Φf_z component, manifests itself as a 20.2 Hz subharmonic. Both data sources, share nearly the same frequency and magnitude at the vortex-shedding frequency and at its subharmonic.

At the high supersonic condition, $M_\infty = 1.70$ (Fig. 18), the vortex-shedding frequency and its subharmonic are shifted to higher values, 54.5 Hz (vs. 40.5 Hz at $M_\infty = 1.18$) and 27.3 Hz (vs. 20.2 Hz at $M_\infty = 1.18$). Especially at station 25, Φf_y based on accelerating-flow data show comparable magnitude peaks at 27.3 Hz and 54.5 Hz. Φf_y based on constant M_∞ data shows predominantly the 54.5 Hz peak and a much smaller peak at the subharmonic frequency and only at station 77.

Differences in the $M_\infty = 1.70$ spectra of Φf_y between constant M_∞ and accelerating-flow data are due to a sensitivity to β of the subharmonic pressure modes. When the vehicle attitude is zero degrees, the f_y forces on the core associated with the left-side and right-side subharmonic pressure modes tend to cancel out. Such is the case for constant $M_\infty = 1.70$

data where, recall, $\alpha = \beta = 0°$ (see Table 2) and, as a result, Φf_y are relatively low near 27 Hz (see Fig. 18a, red curves). In the accelerating-flow case, $\beta = -0.3°$ (Table 2) and the left- and right-side pressure modes associated with the vortex-shedding subharmonic have different strengths, therefore f_y do not cancel as well, causing exceedences shown in Fig. 18a.

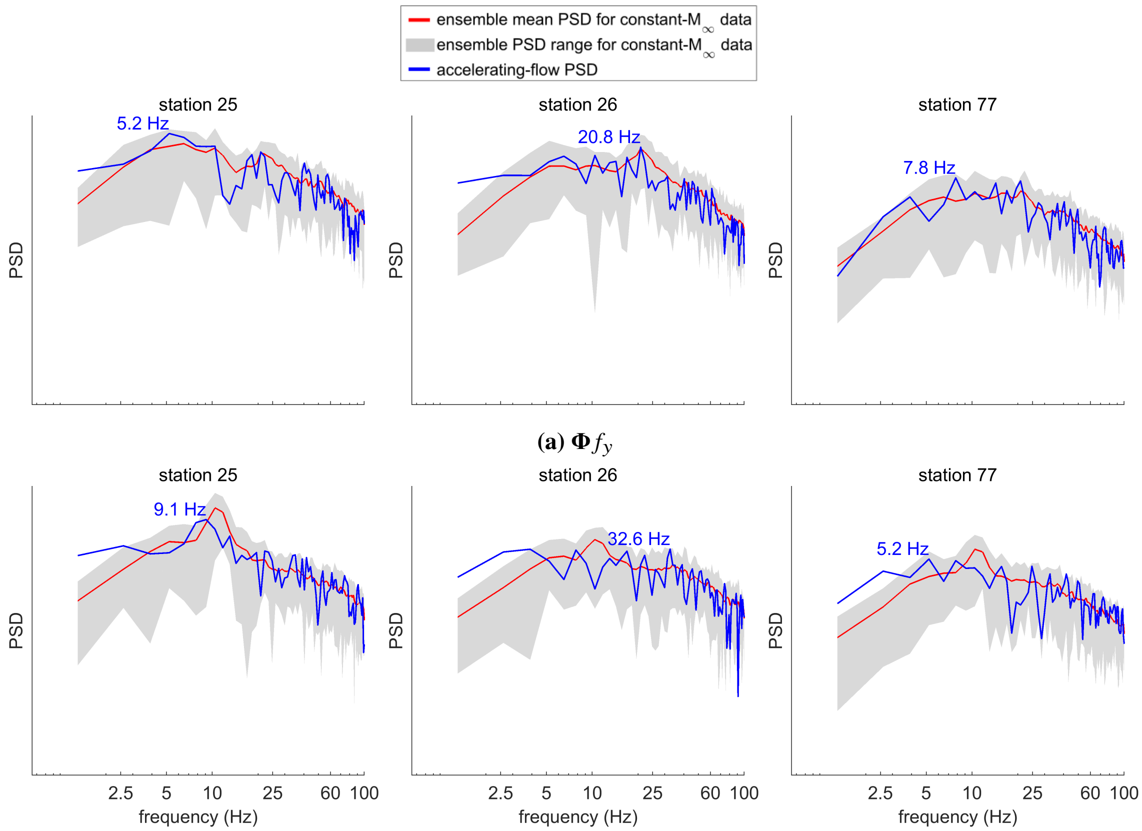

(a) Φf_y

(b) Φf_z

Fig. 16 Comparison of $\Phi f_{y,z}$ based on FUN3D constant M_∞ and accelerating-flow simulations. $M_\infty = 0.95$.

IV. Conclusions

Results are presented from time accurate CFD simulations of the transonic and supersonic flow around the SLS Block 1 vehicle. The purpose of these simulations was to develop a database of buffet forcing functions to be utilized for structural analysis of the vehicle. While buffet forcing functions are typically based on wind-tunnel tests that are performed at constant freestream velocity, CFD was utilized to simulate the changing velocity and attitude experienced by the SLS vehicle during the Artemis I flight. In these simulations, referred to as accelerating-flow, the freestream Mach number, M_∞, varied between 0.80 and 1.92. Data collection surfaces focused on a region of the vehicle located downstream of the forward attachment hardware that connects the core stage and the solid rocket boosters. Fluctuating pressures associated with bluff body flow are observed in this region.

The accelerating-flow CFD surface pressures were compared to those measured by pressure transducers instrumented on the Artemis I flight test vehicle. In such an endeavor, it was important to recall that both flight and accelerating-flow simulations are single realizations of the nonstationary flow around the SLS. More accurate comparisons than those presented here require ensemble statistics based on multiple flights and simulations. Nevertheless, at sample locations on the core intertank and liquid hydrogen tank, simulated and flight-measured C'_p time histories shared comparable peak-to-peak magnitudes over a freestream Mach number range. Likewise, moving-window rms trends are in agreement between accelerating-flow CFD and flight data although, at specific M_∞ values, somewhat larger percent differences in $C'_{p,\mathrm{rms}}$ exist. In terms of coherence, accelerating-flow CFD and AR01 data have comparable longitudinal and azimuthal

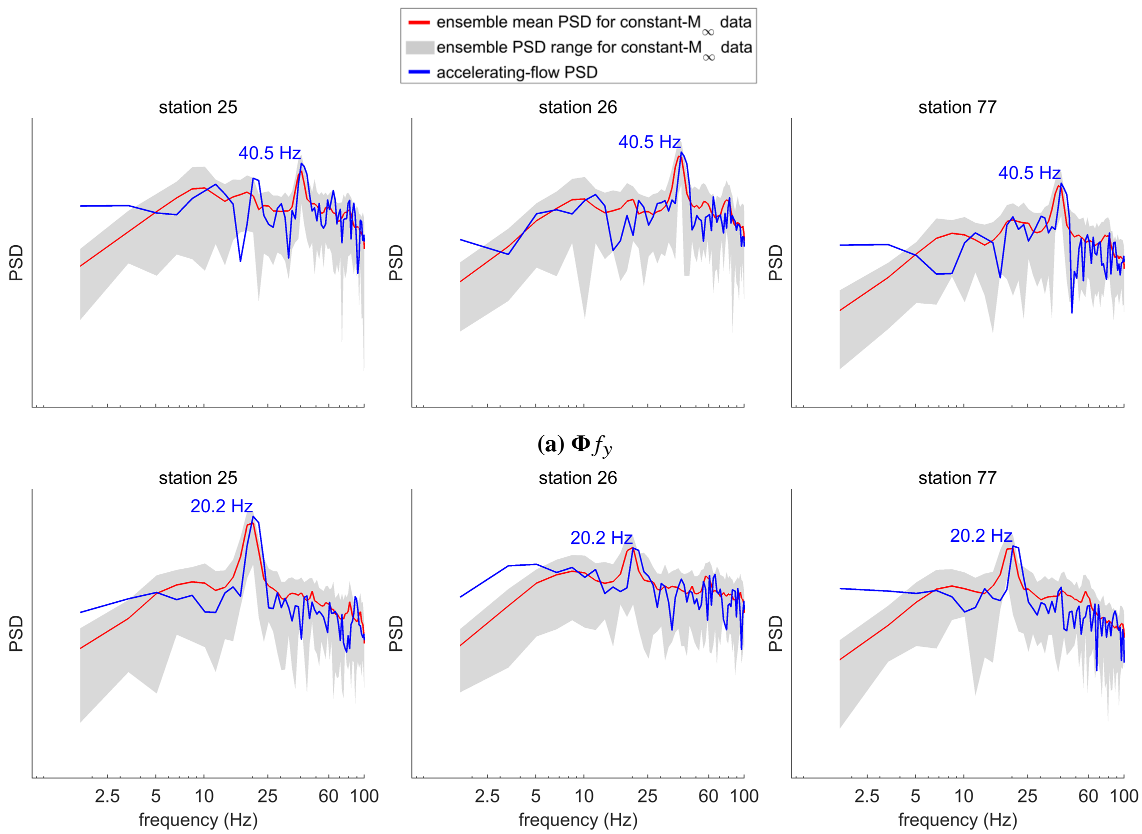

(a) Φf_y

(b) Φf_z

Fig. 17 Comparison of $\Phi f_{y,z}$ based on FUN3D constant M_∞ and accelerating-flow simulations. M_∞ = 1.18.

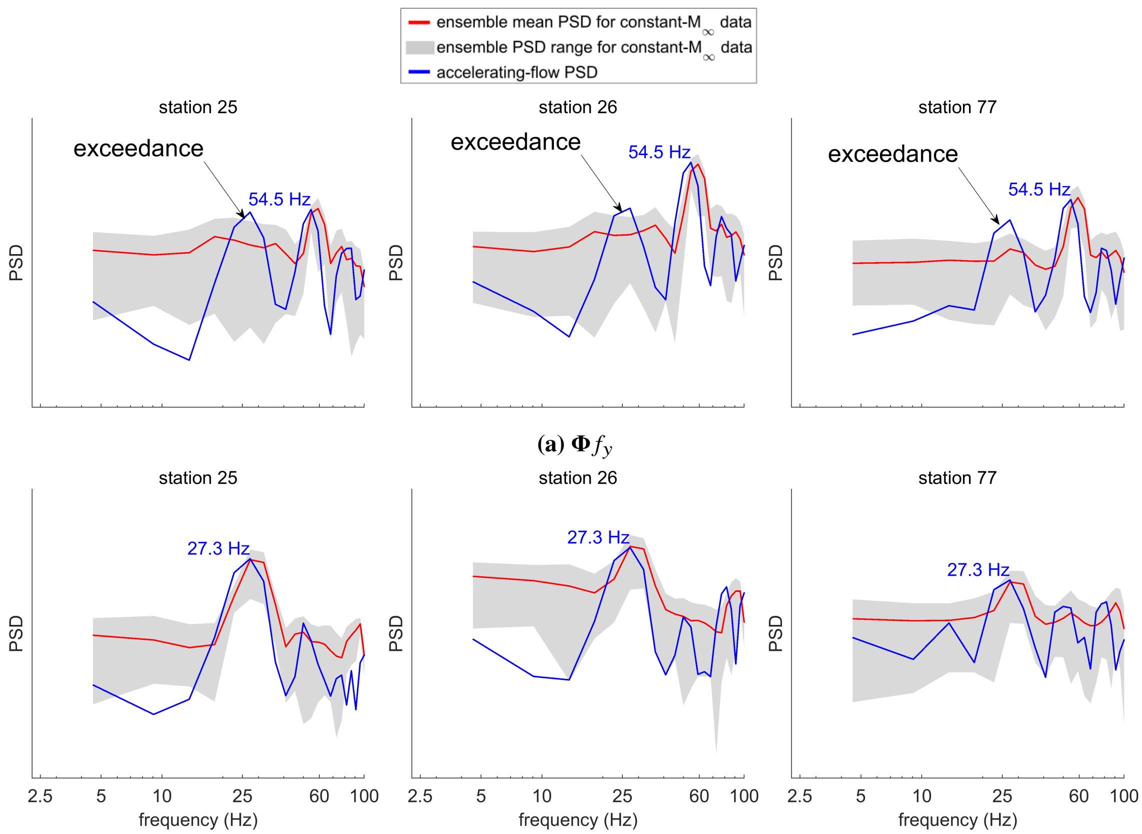

(a) Φf_y

(b) Φf_z

Fig. 18 Comparison of $\Phi f_{y,z}$ based on FUN3D constant M_∞ and accelerating-flow simulations. M_∞ = 1.70.

coherence function trends vs. frequency between fluctuating pressures at sample locations in the core-LSRB gap and on the RSRB.

The frequency content of C_p' revealed similar features between accelerating-flow CFD and flight data. Specifically, CFD captured the narrowband frequencies associated with vortex shedding off the forward attachment hardware. Notably, accelerating-flow CFD showed a rapid rise in vortex shedding frequencies that was observed in the flight data near $M_\infty = 1.70$. In contrast, SLS wind-tunnel data at supersonic Mach numbers (not presented in this paper) show linearly increasing vortex-shedding frequencies with freestream velocity—a discrepancy that is being reexamined.

On the basis of favorable comparisons between accelerating-flow simulations and Artemis I data, the CFD-based fluctuating pressures were integrated into orthogonal force components acting at stations on the core and solid rocket boosters. Such fluctuating forces are referred to as buffet forcing functions and form the basis of a CFD-based BFF database. These BFFs were presented in sectional form, i.e., forces per unit length. A key objective was to investigate any potential difference between BFFs that account for the effects of vehicle acceleration vs. BFFs that are based on constant freestream conditions, i.e., such as those established in wind tunnels. For this purpose, a set of additional time accurate CFD simulations were conducted at constant freestream conditions corresponding to $M_\infty = 0.95, 1.18, 1.70$.

To make meaningful comparisons, BFF samples from the accelerating-flow simulations were windowed within $M_\infty \pm 0.01$, where $M_\infty = 0.95, 1.18, 1.70$. Based on this windowing approach, the rms of the sectional BFFs compared very well between accelerating-flow and constant M_∞ simulations for the three reference Mach numbers. A notable difference exists at $M_\infty = 0.95$ due to causes that are under investigation. Estimates of the probability distribution of the sectional forces rms were obtained based on constant M_∞ CFD. As expected, for transonic conditions, in the peak buffet environment region, there is a wider distribution of sectional force rms compared to supersonic conditions.

The power spectral density of the sectional forces, Φf_i, was assessed for both accelerating-flow and constant M_∞ data. In most cases, Φf_i based on accelerating-flow data are enveloped by a range of Φf_i based on constant M_∞ data. Below 10 Hz, accelerating-flow Φf_i exceeds or is less than this range depending on the freestream Mach number. At $M_\infty = 1.70$, accelerating-flow Φf_y exceeds its constant Mach number CFD counterpart at a subharmonic of vortex shedding. This exceedence is due to a sensitivity to β of the unsteady pressure mode of the subharmonic. In the constant $M_\infty = 1.70$ simulation, the vehicle attitude is zero degrees and the f_y forces on the core associated with the left-side and right-side subharmonic pressure modes tend to cancel out. In the accelerating-flow case, due to a nonzero β value, the left- and right-side pressure modes associated with the vortex-shedding subharmonic have different strengths, therefore f_y do not cancel out as well, causing Φf_y exceedences relative to constant M_∞ data.

In conclusion, accelerating-flow CFD provides a satisfactory estimation of the Artemis I peak buffet environment. Buffet forcing functions that are derived from flight-like simulations, which include the effects of vehicle acceleration, are well represented by BFFs based on wind-tunnel-like simulations that assume stationary flow conditions. Future work could investigate how the pressure field spatial resolution impacts the present accelerating-flow BFF database.

References

[1] NASA.gov, "Space Launch System," , 2024. URL https://www.nasa.gov/humans-in-space/space-launch-system/, accessed: NOV, 2024.

[2] NASA.gov, "SLS Lift Capabilities and Configurations," , 2024. URL https://www.nasa.gov/sites/default/files/atoms/files/sls_lift_capabilities_and_configurations_508_08202018_0.pdf,, accessed: NOV, 2024.

[3] NASA.gov, "Around the Moon with NASA's First Launch of SLS with Orion," , 2022. URL https://www.nasa.gov/feature/around-the-moon-with-nasa-s-first-launch-of-sls-with-orion, accessed: NOV, 2024.

[4] Piatak, D. J., Sekula, M. K., Rausch, R., Florance, J. R., and Ivanco, T. G., "Overview of the Space Launch System Transonic Buffet Environment Test Program," *53rd AIAA Aerospace Sciences Meeting, AIAA SciTech Forum*, 2015. doi: 10.2514/6.2015-0557.

[5] Sekula, M. K., Piatak, D. J., and Rausch, R. D., "Space Launch System Program (SLSP) Vehicle Aerodynamic Substantion Report for the SLS-1000X Buffet Forcing Function Database," NASA TM-2018-21930, May 2018.

[6] Heaney, P. S., Sekula, M. K., Piatak, D. J., Ramey, J. M., and Soranna, F., "Evaluation of Preliminary Buffet Forcing Function Development based on Wind-Tunnel Tests of Geometrically-similar Models," *AIAA Aviation 2020 Forum*, 2020. doi:10.2514/6.2020-2669, URL https://arc.aiaa.org/doi/abs/10.2514/6.2020-2669.

[7] Heaney, P. S., Piatak, D. J., Goushcha, O., Ramey, J. M., Soranna, F., and Sekula, M. K., "Comparison of Wind-Tunnel and Flight Unsteady Pressure Stochastic Characteristics for the Space Launch System Artemis I Flight," *AIAA SciTech 2024 Forum*, 2024. doi:10.2514/6.2024-0019, URL https://arc.aiaa.org/doi/abs/10.2514/6.2024-0019.

[8] Soranna, F., Heaney, P. S., Sekula, M. K., Piatak, D. J., Goushcha, O. O., Ramey, J. M., Swatzell, S. R., and Griggs, L. G., "Artemis I Versus Wind-Tunnel Buffet-Induced Forces and Structural Responses," *Journal of Spacecraft and Rockets*, Vol. 61, No. 5, 2024, pp. 1375–1390. doi:10.2514/1.A36054, URL https://doi.org/10.2514/1.A36054.

[9] Ragab, M. M., "Buffet loads prediction for a launch vehicle and comparison to flight data," *Journal of Spacecraft and Rockets*, Vol. 29, No. 6, 1992, pp. 849–855. doi:10.2514/3.25541, URL https://doi.org/10.2514/3.25541.

[10] Piatak, D. J., Sekula, M. K., and Rausch, R. D., "Comparison of Ares I-X Wind-Tunnel-Derived Buffet Environment with Flight Data," *Journal of Spacecraft and Rockets*, Vol. 49, No. 5, 2012, pp. 822–833. doi:10.2514/1.A32176, URL https://doi.org/10.2514/1.A32176.

[11] Atkins, T., Casiano, M. J., Gillespie, D. M., Honeycutt, T., Goushcha, O., Heaney, P. S., Ramey, J. M., Piatak, D. J., Sekula, M. K., and Soranna, F., "Artemis I Developmental Flight Instrumentation Data Quality Assessment and Processing," *AIAA SciTech 2024*, 2024.

[12] Anderson, W. K., Biedron, R. T., Carlson, J.-R., Derlaga, J. M., Diskin, B., Druyor, C. T., Gnoffo, P. A., Hammond, D. P., Jacobson, K. E., Jones, W. T., Kleb, B., Lee-Rausch, E. M., Liu, Y., Nastac, G. C., Nielsen, E. J., Padway, E. M., Park, M. A., Rumsey, C. L., Thomas, J. L., Thompson, K. B., Walden, A. C., Wang, L., Wood, S. L., Wood, W. A., and Zhang, X., "FUN3D 14.0.2 Manual," Tech. Rep. TM-20230004211, NASA, November 2023. URL https://fun3d.larc.nasa.gov/.

[13] Brauckmann, G. J., Streett, C., Kleb, W. L., Alter, S. J., Murphy, K. J., and Glass, C., "Computational and Experimental Unsteady Pressures for Alternate SLS Booster Nose Shapes," *53rd AIAA Aerospace Sciences Meeting*, 2015. doi:10.2514/6.2015-0559, URL https://arc.aiaa.org/doi/abs/10.2514/6.2015-0559.

[14] Goushcha, O., "Developmental Flight Instrumentation: Review of Space Shuttle, Ares I-X, and Artemis I," *AIAA SciTech 2024 Forum*, 2024. doi:10.2514/6.2024-0014, URL https://arc.aiaa.org/doi/abs/10.2514/6.2024-0014.

[15] Heaney, P. S., Piatak, D. J., Sekula, M. K., and Soranna, F., "Comparison of Wind-Tunnel and Flight Unsteady Pressure Environments for the Ares I-X Flight Test Vehicle," *AIAA SciTech 2022 Forum*, 2022. doi:10.2514/6.2022-2413, URL https://arc.aiaa.org/doi/abs/10.2514/6.2022-2413.

[16] Hoffmann, H., "Violin Plot version: Version 1.7.0.0," , 2015. URL https://www.mathworks.com/matlabcentral/fileexchange/45134-violin-plot.